PAPER

Check for updates

The Li$_2$Ti$_6$O$_{13}$ and Li$_2$Zr$_6$O$_{13}$ composite as a high-performance anode for alkali-ion batteries: a molecular dynamics study†

Yohandys A. Zulueta, [ID] [a] Minh Tho Nguyen [ID] *[bc] and My Phuong Pham-Ho [ID] [de]

The current development of technology has highlighted the necessity of compounds that enhance the durability and performance of alkali-ion batteries. The anodes of these batteries need to overcome the challenges of low dc-conductivity at ambient temperatures and interfacial resistance between the solid-state electrolyte. By conducting large-scale molecular dynamics simulations, we investigated the transport properties of Li$_2$Ti$_6$O$_{13}$ and Li$_2$Zr$_6$O$_{13}$ mono- and bi-crystals, as well as Li$_2$Ti$_6$O$_{13}$@Li$_2$Zr$_6$O$_{13}$ composites. While the monocrystalline and bi-crystalline Li$_2$Zr$_6$O$_{13}$ show similar transport properties, the composite materials, combining both compounds, exhibit the highest diffusion coefficients and dc-conductivity. The transport properties of the composite materials are found to be significantly higher than those mono- and bi-crystalline samples due to the Li interstitial mechanism and the presence of grain boundaries. Our study offers valuable insights for the development of high-performance energy storage materials.

1. Introduction

Lithium hexatitanate (Li$_2$Ti$_6$O$_{13}$) is one of the materials that can be used as a negative electrode in lithium ion batteries (LIBs). Li$_2$Ti$_6$O$_{13}$ has a tunnel structure with a large surface area, a theoretical capacity of 170 mA h g^{-1}, open cell voltage of 1.5–1.7 V and dc conductivity at 25 °C of 5.6×10^{-6} S cm^{-1}. These structural and electrochemical properties make this compound an intriguing anode material.[1–5] Despite such intrinsic properties, many experimental strategies were considered to improve the anode performance, and it appears that Li$_2$Ti$_6$O$_{13}$ is less promising than lithium pentatitanate (Li$_4$Ti$_5$O$_{12}$) for use as a anode.[1–6]

In a previous work, a new compound, lithium hexazirconate (Li$_2$Zr$_6$O$_{13}$), and its anode performance were studied by using

*a*Departamento de Física, Facultad de Ciencias Naturales y Exactas, Universidad de Oriente, Santiago de Cuba, CP 90500, Cuba

*b*Laboratory for Chemical Computation and Modeling, Institute for Computational Science and Artificial Intelligence, Van Lang University, Ho Chi Minh City, Vietnam. E-mail: minhtho.nguyen@vlu.edu.vn

*c*Faculty of Applied Technology, School of Technology, Van Lang University, Ho Chi Minh City, Vietnam

*d*Faculty of Chemical Engineering, Ho Chi Minh City University of Technology (HCMUT), 268 Ly Thuong Kiet Street, District 10, Ho Chi Minh City, Vietnam

*e*Vietnam National University Ho Chi Minh City, Linh Trung Ward, Thu Duc City, Ho Chi Minh City, Vietnam

† Electronic supplementary information (ESI) available: LAMMPS input files of mono, bi-crystalline Li$_2$Zr$_6$O$_{13}$ samples, and Li$_2$Zr$_6$O$_{13}$@Li$_2$Ti$_6$O$_{13}$ composite for reproducibility providing further simulation details for the readers. See DOI: https://doi.org/10.1039/d4ra02998d

density functional theory computations.[5] The Li$_2$Zr$_6$O$_{13}$ possesses the lattice structure of Li$_2$Ti$_6$O$_{13}$, including the lattice, electronic and mechanical properties. The open cell voltage of Li$_2$Zr$_6$O$_{13}$ is close to the reported value for Li$_2$Ti$_6$O$_{13}$ and other anode materials.[1–5,7] Various experimental strategies have been devoted to improve the performance of similarly active materials for anodes.[1–12] For instance, Li$_2$TiO$_3$ was used as a co-material to stabilize the structure and enhance the electrode material with better electrochemical performance of the combined Li$_4$Ti$_5$O$_{12}$–Li$_2$TiO$_3$ whose ionic conductivity is higher than that of Li$_4$Ti$_5$O$_{12}$.[8,9] Carbon-coating free, β-Li$_2$TiO$_3$ delivers a specific capacity of 200 mA h g^{-1} within 100 cycles and 170 mA h g^{-1} after 500 cycles preserving a coulombic efficiency above 97%.[10] Graphene supported Li$_2$SiO$_3$/Li$_2$SnO$_3$ prepared through a hydrothermal method has an initial specific capacity of 1016.5 mA h g^{-1} and its specific capacity amounts to 440.8 mA h g^{-1} after 200 cycles. The enhancement of lithium storage of this composite was explained by the synergy among the composite components.[11] In addition, the temperature dependence of electrical properties of composites formed by biphasic sodium titanate and poly(o-methoxyaniline) (Na$_2$Ti$_3$O$_7$/Na$_2$Ti$_6$O$_{13}$/POMA) with different concentrations of POMA was determined from complex impedance measurements.[12] Differences on the electrical properties between the composite and individual components were reported.[12]

In this context we set out to search for a co-material which can be combined with Li$_2$Ti$_6$O$_{13}$ using molecular dynamics simulations. In fact, atomistic simulation is a powerful tool to investigate structure–property relations and for theoretical

design of new materials.[13–16] In particular, classical molecular dynamics computations provide us with relevant information concerning the transport properties in large systems.[13–16]

The nudged elastic band (NEB) method and molecular dynamics (MD) simulations are popular computational methods used to investigate the behaviour of molecules and materials at the atomic level. The main difference between the two methods consists in the fact that NEB computations are used to evaluate the energy barriers and reaction pathways between different stable states, whereas MD is used to probe the behaviour of materials over time and their dynamic behaviour. In addition, MD computations allow the investigation of very large molecular systems including the polycrystalline materials.

Various theoretical studies on $Li_2Ti_6O_{13}$ have been reported, disclosing its thermodynamic stability, lattice properties, doping effect, and partially diffusion process.[5,7,17–19] To our knowledge, full molecular dynamics simulations disclosing the transport properties of $Li_2Ti_6O_{13}$ have not been reported yet. To further understand the factors influencing the electrochemical behaviour, the transport properties are essential keys for determine the Li insertion/de-insertion rates.

Transport properties depend not only on the atomic mass and net charge of the mobile, but also on the migration path and the proper structure of the system. It is well-known that the effect of grain boundary is important on transport properties in polycrystalline materials.[20–22] In the present study, we conduct large-scale MD computations with the aim to disclose transport properties of both mono- and bi-crystalline $Li_2B_6O_{13}$ with the metal B = Ti, Zr, and as mentioned above, of a new ceramic composite materials combining for the first time both $Li_2Ti_6O_{13}$ and $Li_2Zr_6O_{13}$ compounds. In particular, the influence of the grain boundary on transport properties are disseminated, providing us with some relevant strategies stimulating future experimental investigations.

2. Computational protocols

Fig. 1 displays the unit cell of the hexa-metaloxide $Li_2B_6O_{13}$ with B = Ti and Zr in the conventional representation. The monoclinic $Li_2B_6O_{13}$ crystal structure consists of a corner-sharing $[BO_6]$ octahedron and a $[LiO_4]$ tetrahedron. The $[BO_6]$ octahedron forms chains along 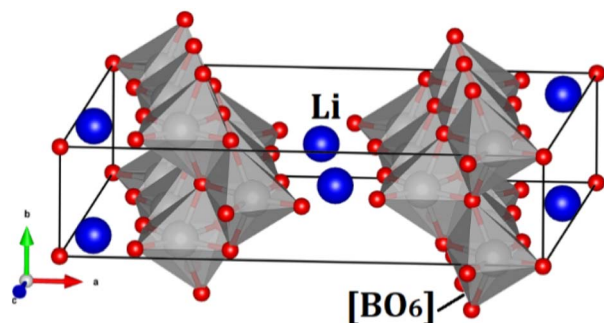the b-axis of the crystal, which are connected by the $[LiO_4]$ tetrahedron to form a three-dimensional (3D) structure. The tunnels running along the b-axis serve as ion channels for lithium ion diffusion.[1–5,7]

High diffusion coefficient and high dc-conductivity, complemented by low activation energies at operative temperatures, are crucial parameters for evaluating potential battery materials as they ensure fast Li transport properties. In fact, the exceptional ion transport properties enable the desirable anode to exhibit better cycling performance, preventing a certain chemical reactivity between the anode and the solid-state electrolyte.[23–27] In this study, the Large-Scale Atomic-Molecular Massively Parallel Simulator (LAMMPS)[28] code is used to perform large-scale MD simulations with periodic boundary conditions to disclose Li^+ transport properties. The potential parameters employed, also known as force fields, are taken from previous reports.[18,29] The Buckingham approximation is used for the short-range interactions, while long-range are purely coulombic describing the long-range potential energy.

Fig. 2 displays the workflow followed in this study. The mono- and bi-crystalline structures of the hexa metal-oxide $Li_2B_6O_{13}$ for both metals B = Ti, Zr, as well as the $Li_2Ti_6O_{13}@Li_2Zr_6O_{13}$ and $Li_2Zr_6O_{13}@Li_2Ti_6O_{13}$ composite samples, are constructed by using the Voronoi tessellation method as compiled in the Atomsk code.[30] For monocrystalline $Li_2Ti_6O_{13}$ ($Li_2Zr_6O_{13}$) samples, we use a supercell containing 360 unit cells ($4 \times 15 \times 6$ unit cells). In this sense, monocrystalline samples consist of a single grain. In contrast, bi-crystalline $Li_2Ti_6O_{13}$ ($Li_2Zr_6O_{13}$) have two randomly oriented grains shown as Grain I and Grain II in Fig. 2.

Regarding composite materials, $Li_2Ti_6O_{13}@Li_2Zr_6O_{13}$ and $Li_2Zr_6O_{13}@Li_2Ti_6O_{13}$, they are constructed from the template of their bi-crystalline simulation boxes. The label (Grain I) @(Grain II) indicates that in $Li_2Ti_6O_{13}@Li_2Zr_6O_{13}$, Grain I consists of $Li_2Ti_6O_{13}$, while Grain II comprises $Li_2Zr_6O_{13}$.

Fig. 1 Conventional representation of the hexa–metal-oxide $Li_2B_6O_{13}$ (B = Ti, Zr) unit cell in the $C2/m$. Blue balls represent the Li ions and the grey polyhedron the $[BO_6]$ octahedron.
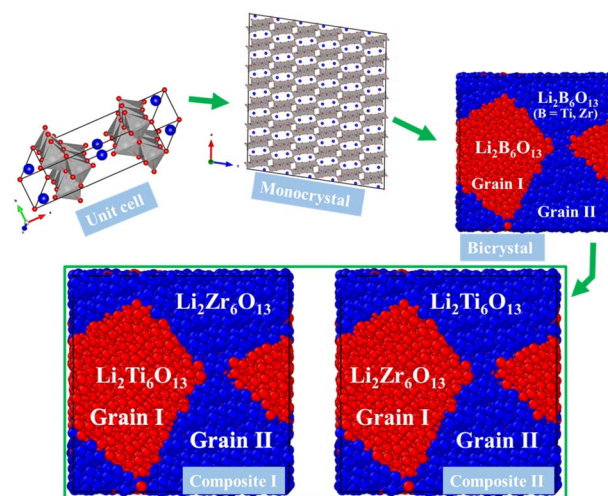

Fig. 2 Workflow describing the construction models used in the present study.

Similarly, for $Li_2Zr_6O_{13}@Li_2Ti_6O_{13}$, Grain I is $Li_2Zr_6O_{13}$, and Grain II is $Li_2Ti_6O_{13}$. In this paper, the term composition refers hereafter to the $Li_2B_6O_{13}$ (B = Ti, Zr) structure present in each grain.

Simulation boxes of $60 \times 60 \times 60$ Å^3 are used for modelling the bi-crystalline and composite samples. To probe the Li$^+$ migration, we introduce low concentration (0.09) of Li$^+$ vacancies compensated by O^{2-} vacancies (in accordance with the Li$_2$O Schottky defect) inside the simulation boxes. The size of simulation boxes for monocrystalline samples, resulting in a $61.71 \times 56.63 \times 55.94$ Å^3, close to the bi-crystalline and composite samples.

During the tessellation process, certain ions are placed too close to each other or even superimposed. As a result, these ions are either removed or separated prior to introducing defects into the bi-crystalline sample. Any extra charge which may arise due to the introduction of defect concentration is compensated by Li$^+$ vacancies.

To ensure the accuracy of the simulation results, the simulation boxes undergo equilibration using an isothermal–isobaric ensemble (NPT). Once equilibrated, constant volume–temperature NVT ensemble is used for production, with the mean square displacement (MSD) for the Li$^+$ ions being saved to calculate their diffusion coefficient (D).

The slope of the MSD plots is used to obtain the diffusion coefficient as follows:

$$MSD = 6Dt \tag{1}$$

where t is the simulation time. For MD simulations, 2 ns with a time step of 2 fs is used for the production run and the temperature ranges between 900–1400 K.

In the ESI,† a sample of LAMMPS input files of mono-, bi-crystalline $Li_2Zr_6O_{13}$ samples, and $Li_2Zr_6O_{13}@Li_2Ti_6O_{13}$ composite are included for reproducibility providing further simulation details for use by the readers.

The diffusion data computed are then converted to the dc-conductivity by using the Nernst–Einstein equation:

$$\sigma(T) = H_V N q^2 D(T)/k_B T \tag{2}$$

where $\sigma(T)$ and $D(T)$ represent the dc-conductivity and diffusion coefficient at the temperature T, respectively, N the charge density of the mobile ion; q is the charge of the mobile ion, k_B the Boltzmann constant and H_V represents the Haven's ratio which considers the effect of the external electric field on the mobility of the charge carrier (ion) in real samples.[13,15,22,29]

We assume $H_V = 1$ due to the lack of experimental measurements of diffusion and conduction processes in these materials, in particular for $Li_2Zr_6O_{13}$. Both the diffusion and conduction processes are thermally activated; it implies that the relevant kinetics follow the conventional Arrhenius equation $\Delta(T) = \Delta_0 \exp(-E_a^\Delta/k_B T)$, where k_B represents the Boltzman constant, T the temperature, Δ_0 the pre-exponential factor ($\Delta(T) \rightarrow \Delta_0$, $T \rightarrow \infty$) and E_a^Δ the activation energy, with $\Delta = D$ the Arrhenius dependence for diffusion can be obtained, while for $\Delta = \sigma$, the conduction process is determined.

Together with the activation energy, the diffusion and dc-conductivity at 25 °C are the magnitudes characterizing the transport properties in ionic materials.[13,15,22,29]

3. Results and discussion

3.1 Tracking Li$^+$-ion in mono-, bi-crystalline $Li_2B_6O_{13}$ (B = Ti, Zr) and $Li_2Ti_6O_{13}@Li_2Zr_6O_{13}$ composite samples

The temporal evolution of MSDs with respect to the temperature of $Li_2Ti_6O_{13}$ and $Li_2Zr_6O_{13}$ are depicted in Fig. 3. As it is shown, the slope of all MSD plots increases with the increment of the temperature, indicating the presence of a thermally activated process. Another interesting finding is that the MSD plots for $Li_2Ti_6O_{13}$ are placed higher than that for $Li_2Zr_6O_{13}$.

The diffusion coefficient, obtained from eqn (1), are thus larger in $Li_2Ti_6O_{13}$ as compared to the monocrystalline $Li_2Zr_6O_{13}$. It can be attributed to the ionic radius difference of 0.115 Å between the Zr^{4+} and Ti^{4+} ions with direct implications

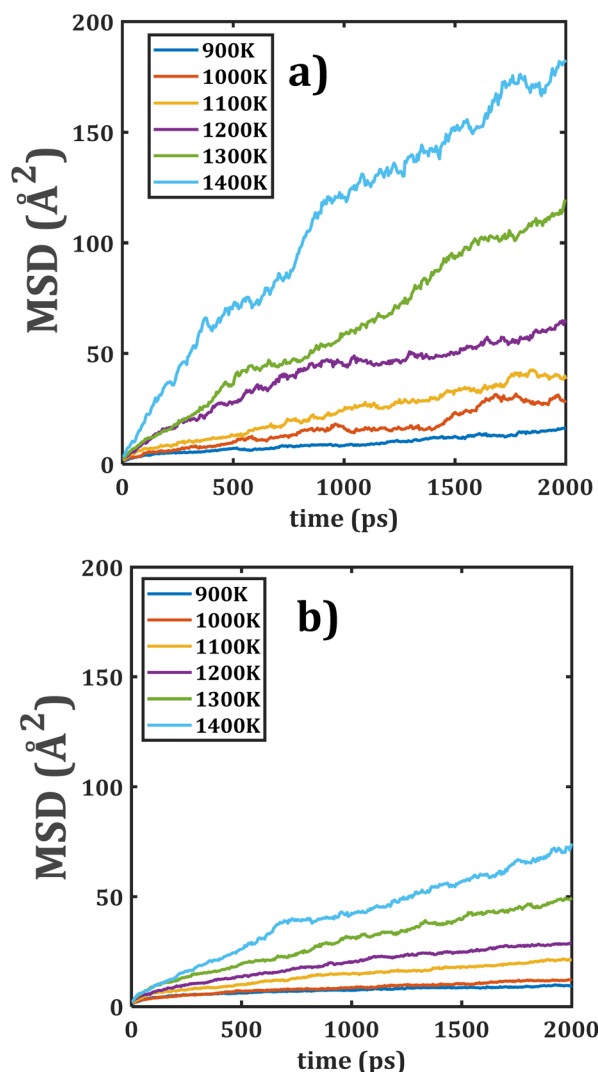Fig. 3 Mean square displacement (MSD) *versus* simulation time of monocrystalline (a) $Li_2Ti_6O_{13}$ and (b) $Li_2Zr_6O_{13}$.

© 2024 The Author(s). Published by the Royal Society of Chemistry

on the structural characteristics such as lattice parameters the [LiO$_4$] space channels, the Li–Li distance, the [BO$_6$] octahedral volume, bond angle variance and average O–O distance.[5,31]

The Li–Li distance is related to the diffusion jump distance where the diffusion mechanism strongly depends on the diffusion jump distance. Li$_2$Zr$_6$O$_{13}$ has longer Li–Li distance as compared to their isostructural Li$_2$Ti$_6$O$_{13}$,[5] in such a way that lower Li$^+$ diffusion coefficients are expected in monocrystalline Li$_2$Zr$_6$O$_{13}$.

Fig. 4 shows the temporal evolution of MSD of the bi-crystalline Li$_2$Ti$_6$O$_{13}$ and Li$_2$Zr$_6$O$_{13}$ samples. In this case, the linear dependence of MSD with respect to time is more appreciable in the entire range of the simulation time; it is ascribed to the presence of grain boundaries.

The grain boundary affects the transport properties introducing additional Li$^+$ vacancies in the sample, thereby favouring the Li$^+$ migration. Analogously, the diffusion characteristic in Li$_2$Ti$_6$O$_{13}$ is better than the one in its Zr counterpart. The

effect of [BO$_6$] octahedral distortion, together with the grain boundaries, are the sources of better transport properties in bi-against monocrystalline samples. [5,20–22]

The next step deals with the Li$^+$ transport properties of the target Li$_2$Ti$_6$O$_{13}$@Li$_2$Zr$_6$O$_{13}$ and Li$_2$Zr$_6$O$_{13}$@Li$_2$Ti$_6$O$_{13}$ composite samples. As was described in Section 2 (and depicted in Fig. 2), the Li$_2$Ti$_6$O$_{13}$@Li$_2$Zr$_6$O$_{13}$ composite consists in a bi-crystal where Grain I contains Li$_2$Ti$_6$O$_{13}$ and Grain II, Li$_2$Zr$_6$O$_{13}$ (denoted as LTZO), while the Li$_2$Zr$_6$O$_{13}$@Li$_2$Ti$_6$O$_{13}$ composite is the inverse: the Grain II contain Li$_2$Ti$_6$O$_{13}$ and Grain I is constituted by Li$_2$Zr$_6$O$_{13}$ (denoted as LZTO).

Fig. 5 displays the MSD plots of both composite materials. Comparison of both MSD versus time points out appreciable similarities between the slopes of each temperature and better linear dependence as compared to the individual monocrystalline samples. These results suggest that a change in the grain composition does not affect the Li$^+$ transport properties in these composite materials.

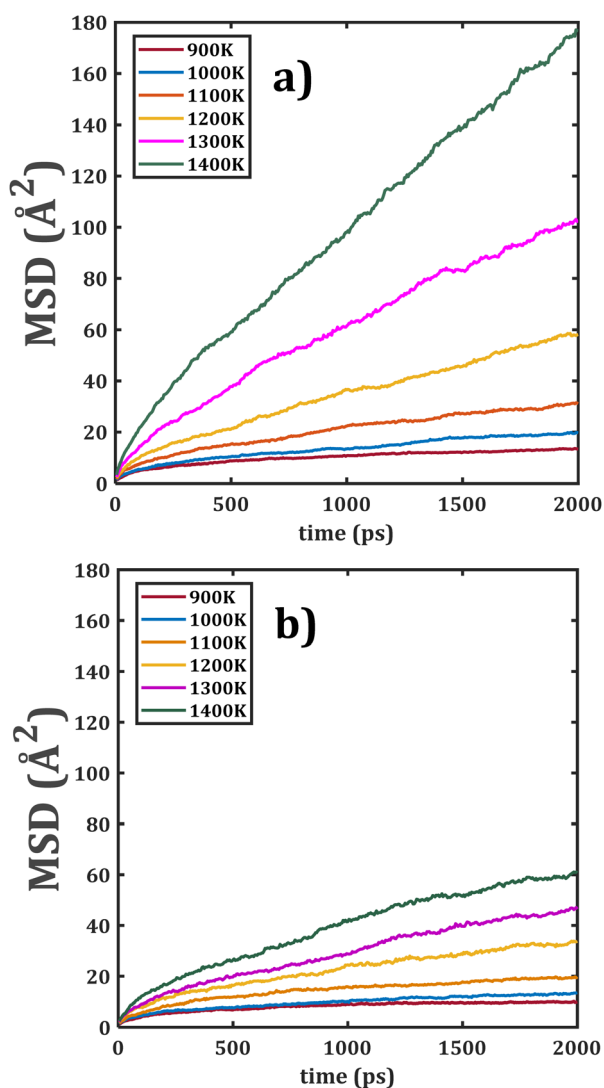Fig. 4 Mean square displacement (MSD) versus simulation time of bicrystalline (a) Li$_2$Ti$_6$O$_{13}$ and (b) Li$_2$Zr$_6$O$_{13}$.
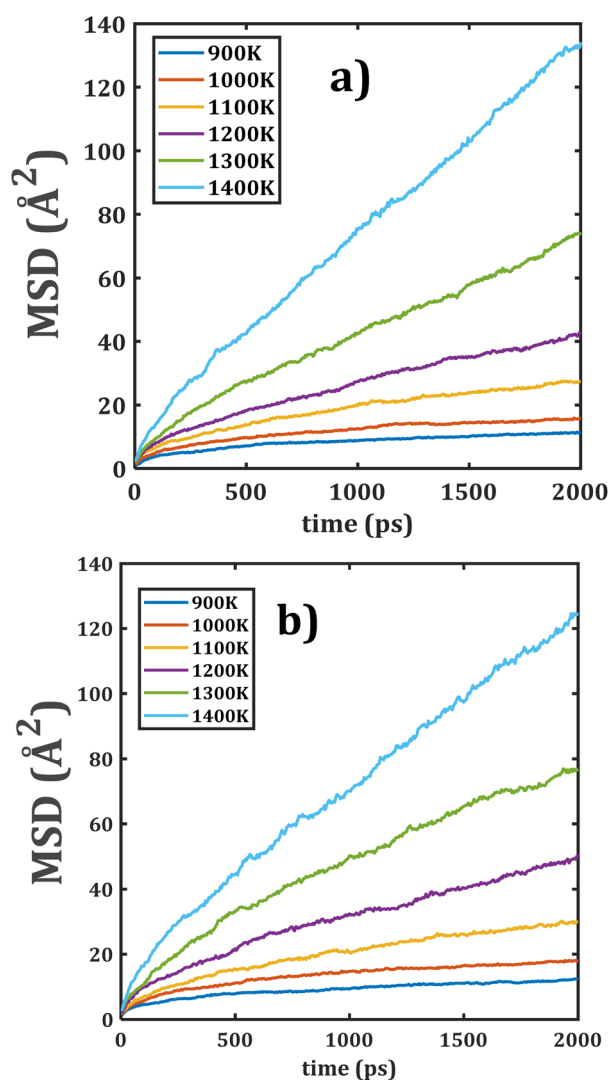
Fig. 5 Mean displacement (MSD) versus simulation time of composite Li$_2$Ti$_6$O$_{13}$@Li$_2$Zr$_6$O$_{13}$ materials: (a) LTZO and (b) LZTO.

3.2 Transport properties of Li$^+$-ion in mono-, bi-crystalline Li$_2$B$_6$O$_{13}$ and composite Li$_2$Ti$_6$O$_{13}$@Li$_2$Zr$_6$O$_{13}$ samples

In order to quantitatively measure the Li$^+$ transport properties of the compounds of interest, the Arrhenius dependence of both diffusion and conduction processes is performed. With the collected diffusion data in each sample, the dc-conductivity at each temperature is obtained by using eqn (2). Fig. 6 displays the Arrhenius dependence of the diffusion and conduction data for each sample. There are various findings concerning the diffusion/conduction behaviour:

- The monocrystalline Li$_2$Zr$_6$O$_{13}$ sample exhibits transport properties similar to those of the bi-crystalline Li$_2$Zr$_6$O$_{13}$ sample.
- Both the largest diffusion coefficients and dc-conductivity are observed in the composite materials, followed by mono-crystalline and bi-crystalline Li$_2$Ti$_6$O$_{13}$ samples.
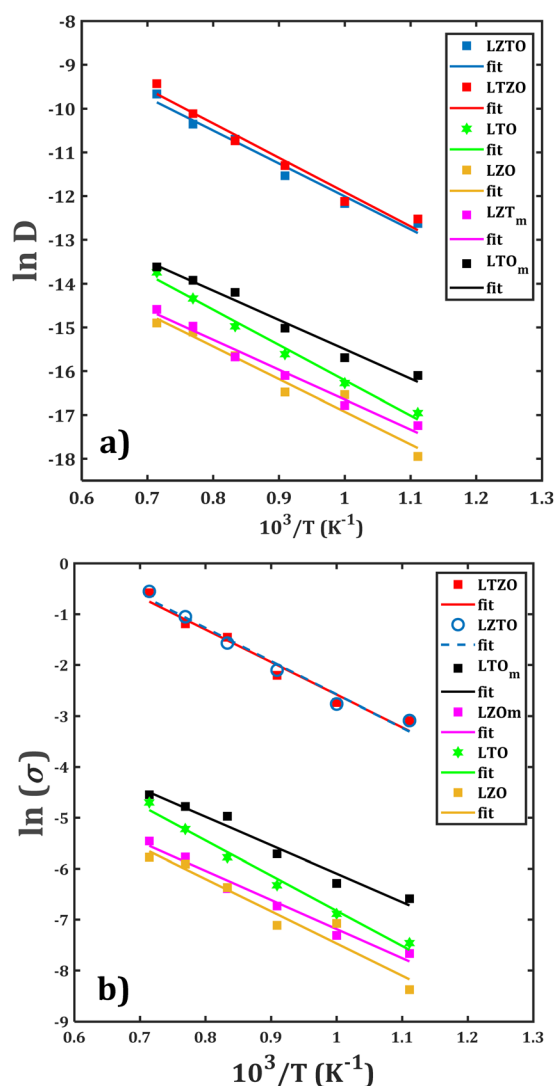

Fig. 6 Arrhenius-type dependence of (a) diffusion coefficient and (b) dc-conductivity with temperature for Li$_2$Ti$_6$O$_{13}$/Li$_2$Zr$_6$O$_{13}$ samples: monocrystalline (LTO$_m$/LZO$_m$), bi-crystalline (LTO/LZO), and composite (LTZO/LZTO). In each case, the lines represent the Arrhenius fit.

- The diffusion coefficients and dc-conductivity for the composite materials are found to be about two orders of magnitude higher as compared to the rest of the samples.

From such a first conclusion, one can assume an insignificant contribution of the grain boundary on the Li$^+$ transport properties of Li$_2$Zr$_6$O$_{13}$. As a matter of fact, the additional Li$^+$ migration sites created by the grain boundaries do not considerably affect the overall Li$^+$ diffusion within the structure. On the other hands, introduction of grain boundary, together with the composition of the composite, tends to improve the Li$^+$ transport properties as compared to those of mono and bi-crystalline samples. In this case, the additional migration sites generated by the grain boundaries result in an alternative Li$^+$ migration paths with shorter diffusion jump distances, thus favouring the diffusion through the composite materials.

Another interesting observation is that the composite has similar values of diffusion coefficient and dc-conductivity upon temperature change, indicating that the composition, *i.e.*, the grain characteristics, does not affect significantly the Li$^+$ mobility. From the results of the Arrhenius fitting, the diffusion activation energy (E_a^D) and the diffusion coefficient at 25 °C ($\tilde{D}$), together with the conduction activation energy (E_a^σ) and conductivity at ambient temperature ($\sigma\tilde{\sigma}$) are determined. Table 1 collects these data calculated for each sample. The obtained activation energy lies between 0.58–0.70 and 0.48–0.56 eV for both diffusion and conduction, respectively. These low values are beneficial for their use as anode materials.[1–12]

The lowest and highest diffusion/conduction activation energy are found for monocrystalline and bi-crystalline Li$_2$Ti$_6$O$_{13}$ samples. The difference of E_a^D and $\tilde{D}$ (E_a^σ and $\sigma\tilde{\sigma}$) between mono- and bi-crystalline Li$_2$Zr$_6$O$_{13}$ is low. In addition, composite materials have similar activation energy and $\tilde{D}$ ($\sigma\tilde{\sigma}$) at ambient temperature. These results consolidate the previous analysis pointing out no influence of grain boundary on the transport properties of Li$_2$Zr$_6$O$_{13}$ as well as the grain composition in the targeted composite materials.

The results of transport properties obtained in this study are in line with those reported in the literature. For instance, values of $\tilde{D}$ ranging between 10^{-9} to 10^{-12} cm^2 s^{-1} have been reported for the knowing anodes Li$_4$Ti$_5$O$_{12}$, Na$_2$Ti$_3$O$_7$ and Na$_2$Ti$_6$O$_{13}$ compounds.[32] Values ranging between 10^{-17} to 10^{-15} cm^2 s^{-1}, in Na$_2$Li$_2$Ti$_6$O$_{14}$ result in a poor performance at high charge–discharge rates were reported.[33–35] Value of conduction activation energy of 0.65 eV was found in a comparative study.[36] Even

Table 1 Activation energy for diffusion (E_a^D) and conduction (E_a^σ) processes and diffusivity ($\tilde{D}$) and conductivity ($\sigma\tilde{\sigma}$) at 25 °C of each compounds

Compound	E_a^D (eV)	$\tilde{D}$ (cm^2 s^{-1})	E_a^σ (eV)	$\sigma\tilde{\sigma}$ (S cm^{-1})
LTO$_m$	0.58	2.96×10^{-14}	0.48	4.84×10^{-9}
LZT$_m$	0.65	1.23×10^{-15}	0.49	1.22×10^{-9}
LTO	0.70	6.10×10^{-16}	0.60	1.05×10^{-10}
LZO	0.64	1.25×10^{-15}	0.55	2.16×10^{-10}
LZTO	0.65	1.20×10^{-13}	0.55	2.43×10^{-8}
LTZO	0.66	1.02×10^{-13}	0.56	1.77×10^{-8}

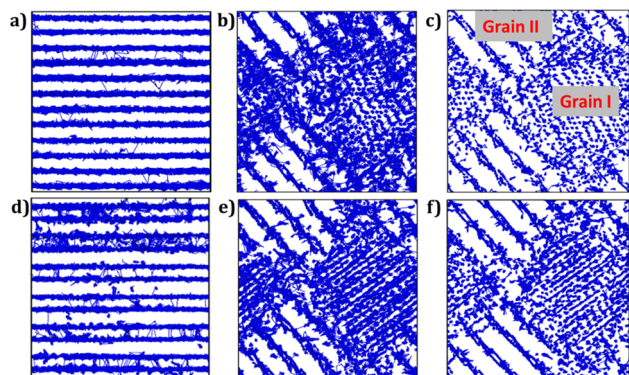**Fig. 7** Li-trajectory density maps (blue lines) of monocrystalline: (a) $Li_2Ti_6O_{13}$, (d) monocrystalline $Li_2Zr_6O_{13}$, bi-crystalline: (b) $Li_2Ti_6O_{13}$, (e) $Li_2Zr_6O_{13}$ and composite: (c) $Li_2Ti_6O_{13}@Li_2Zr_6O_{13}$, (f) $Li_2Zr_6O_{13}@Li_2Ti_6O_{13}$ samples.

a lower value of Li^+ diffusion activation energy (0.47 eV) had been reported with a different theoretical approach.[17]

Fig. 7 illustrates the trajectory density plots of each sample at 900 K for monoclinic and bi-crystalline samples, and for the composite material, the trajectory density plots are recorded at 500 K to better observe the role of the composition at lower temperatures. From Fig. 7a and d, it is observed that the Li^+ migration occurs along the $[LiO_4]$ channels in monoclinic $Li_2Ti_6O_{13}$ and $Li_2Zr_6O_{13}$ samples, including migration between layers. Higher density plot is observed in monocrystalline $Li_2Zr_6O_{13}$ as compared to $Li_2Ti_6O_{13}$. In addition, Li^+ ions migrate *via* an interstitial mechanism, as evidenced by density plots between $[LiO_4]$ layers in agreement with the lower diffusion activation energy in monocrystalline $Li_2Zr_6O_{13}$.

For bi-crystalline samples (Fig. 7b and e), larger density plots are observed, including migration between grain boundaries.

The trajectory density plots of composite materials are very similar to each other, which is also confirmed by their activation energies. In this case, the most relevant findings consist of the evidence of large-scale Li^+ migration across the entire composite, irrespective of the grain composition. After all, the presence of grain boundaries and interstitial mechanism improve the transport properties of these materials.

4. Concluding remarks

Large-scale molecular dynamics simulations are performed to explore the transport properties of mono- and bi-crystalline $Li_2B_6O_{13}$ (B = Ti, Zr) and the composite $Li_2Ti_6O_{13}@Li_2Zr_6O_{13}$. Calculated results demonstrate that the monocrystalline $Li_2Zr_6O_{13}$ exhibits similar transport properties as the bi-crystalline $Li_2Zr_6O_{13}$ sample. The highest diffusion coefficients and dc-conductivity are obtained in the composite material, followed by monocrystalline and bi-crystalline $Li_2Ti_6O_{13}$ samples. The obtained activation energies amount to the range of 0.58–0.70 and 0.48–0.56 eV for both diffusion and conduction, respectively.

The diffusion coefficients and dc-conductivity for the composite material are found to be about two orders of

magnitude higher as compared to the rest of the samples. The trajectory density maps indicate that the Li interstitial mechanism, together with the presence of grain boundaries, are the sources for improvement of transport properties of the composite material.

Considering the much improved transport properties revealed in this study, further experimental verification is highly recommended to assess the potential of these compounds, especially the new composites, as active materials for anodes in the current and future energy storage devices. This also suggests a more general strategy for improvement making use of composite materials.

Data availability

The data supporting this article have been included as part of the ESI.†

Author contributions

Conflicts of interest

There are no conflicts to declare.

Acknowledgements

Notes and references

1 J. C. Pérez-Flores, F. García-Alvarado, M. Hoelzel, I. Sobrados, J. Sanz and A. Kuhn, *Dalton Trans.*, 2012, **41**, 14633–14642.

2 J. C. Pérez-Flores, C. Baehtz, M. Hoelzel, A. Kuhn and F. García-Alvarado, *Phys. Chem. Chem. Phys.*, 2012, **14**, 2892–2899.

3 J. C. Pérez Flores, M. Hoelzel, A. Kuhn and F. García Alvarado, *ECS Trans.*, 2012, **41**, 195–206; J. Zheng, Y. Wu, Y. Sun, J. Rong, H. Li and L. Niu, *Nano-Micro Lett.*, 2021, **13**, 1–37.

4 K. Kataoka, J. Awaka, N. Kijima, H. Hayakawa, K. I. Ohshima and J. Akimoto, *Chem. Mater.*, 2011, **23**, 2344–2352.

5 J. R. Fernández-Gamboa, F. Tielens and Y. A. Zulueta, *Mater. Sci. Semicond. Process.*, 2024, **173**, 108144.

6 B. Vikram Babu, K. Vijaya Babu, G. Tewodros Aregai, L. Seeta Devi, B. Madhavi Latha, M. Sushma Reddi, K. Samatha and V. Veeraiah, *Results Phys.*, 2018, **9**, 284–289.

7 J. R. Fernández-Gamboa, F. Tielens and Y. A. Zulueta, *Mater. Sci. Semicond. Process.*, 2022, **152**, 107074.

8 Y. Wang, A. Zhou, X. Dai, L. Feng, J. Lie and J. Li, *J. Power Sources*, 2014, **266**, 114–120.

9 A. Kozlova, N. Uvarov, M. Sharafutdinov, E. Gerasimov and Y. Mateyshina, *J. Solid State Chem.*, 2022, **313**, 123302.

10 Y. Xie, Q. Wang, F. Gu, K. Dai, M. Shui and J. Shu, *J. Alloys Compd.*, 2022, **893**, 162348.

11 Q. Wang, S. Yang, J. Miao, Y. Zhang, D. Zhang, Y. Chen and Z. Li, *Appl. Surf. Sci.*, 2019, **469**, 253–261.

12 S. Dos Santos Costa, J. Pereira da Silva, M. Moraes Biondo, E. A. Sanches, M. M. Da Silva Paula, F. Xavier Nobre, J. Anglada Rivera, Y. Alexis Zulueta, M. S. Torikachvili, D. Vieira Sampaio, M. Vinicius Dias Vermelho, Ş. Ţălu, L. Aguilera Dominguez and Y. Leyet, *Molecules*, 2022, **27**, 5756.

13 Y. A. Zulueta and M. T. Nguyen, *Phys. Chem. Chem. Phys.*, 2023, **25**, 27926–27935.

14 B. A. Goldmann, M. J. Clarke, J. A. Dawson and M. S. Islam, *J. Mater. Chem. A*, 2022, **10**, 2249–2255.

15 T. Famprikis, P. Canepa, J. A. Dawson, M. S. Islam and C. Masquelier, *Nat. Mater.*, 2019, **18**, 1278–1291.

16 Y. Huang, B. Cao, Z. Geng and H. Li, *Acc. Mater. Res.*, 2024, **5**(2), 184–193.

17 Y. A. Zulueta, P. Geerlings, F. Tielens and M. T. Nguyen, *J. Solid State Chem.*, 2019, **279**, 120930.

18 N. Kuganathan, S. Ganeshalingam and A. Chroneos, *Materials*, 2019, **12**, 2851.

19 Y. A. Zulueta and M. T. Nguyen, *Phys. Status Solidi B*, 2018, **255**, 1700669.

20 J. A. Dawson, P. Canepa, T. Famprikis, C. Masquelier and M. S. Islam, *J. Am. Chem. Soc.*, 2018, **140**, 362–368.

21 J. A. Dawson, H. Chen and M. Saiful Islam, *J. Phys. Chem. C*, 2018, **122**, 23978–23984.

22 L. Van Duong, M. T. Nguyen and Y. A. Zulueta, *RSC Adv.*, 2022, **12**, 20029–20036.

23 A. Ahniyaz, I. de Meatza, A. Kvasha, O. Garcia-Calvo, I. Ahmed, M. F. Sgroi, M. Giuliano, M. Dotoli, M. A. Dumitrescu, M. Jahn and N. Zhang, *Adv. Appl. Energy*, 2021, **4**, 100070.

24 M. Armand and J. M. Tarascon, *Nature*, 2008, **451**, 652–657.

25 Z. H. Fu, X. Chen and Q. Zhang, *Wiley Interdiscip. Rev.: Comput. Mol. Sci.*, 2023, **13**, e1621.

26 H. Cheng, J. G. Shapter, Y. Li and G. Gao, *J. Energy Chem.*, 2021, **57**, 451–468.

27 P. U. Nzereogu, A. D. Omah, F. I. Ezema, E. I. Iwuoha and A. C. Nwanya, *Appl. Surf. Sci. Adv.*, 2022, **9**, 100233.

28 S. Plimpton, *J. Comput. Phys.*, 1995, **117**, 1–19.

29 Y. A. Zulueta and M. T. Nguyen, *Dalton Trans.*, 2021, **50**, 3020–3026.

30 P. Hirel, *Comput. Phys. Commun.*, 2015, **197**, 212–219.

31 R. D. Shannon, *Acta Crystallogr., Sect. A: Cryst. Phys., Diffr., Theor. Gen. Crystallogr.*, 1976, **32**, 751–767.

32 S. Chauque, C. B. Robledo, E. P. M. Leiva, F. Y. Oliva and O. R. Cámara, *ECS Trans.*, 2014, **63**, 113–128.

33 P. Wang, P. Li, T. F. Yi, X. Lin, H. Yu, Y. R. Zhu, S. Qian, M. Shui and J. Shu, *J. Power Sources*, 2015, **297**, 283–294.

34 K. Wu, D. Wang, X. Lin, L. Shao, M. Shui, X. Jiang, N. Long, Y. Ren and J. Shu, *J. Electroanal. Chem.*, 2014, **717–718**, 10–16.

35 P. Wang, P. Li, T. F. Yi, X. Lin, Y. R. Zhu, L. Shao, M. Shui, N. Long and J. Shu, *J. Power Sources*, 2015, **293**, 33–41.

36 O. Skurikhina, M. Gombotz, M. Senna, M. Fabián, M. Baláz, K. L. Da Silva, M. Achimovičová, H. M. R. Wilkening and B. Gadermaier, *Z. Phys. Chem.*, 2022, **236**, 1077–1088.